Conference Paper, Published Version

Leschka, Stefan; Oumeraci, Hocine

Source Term Formulae to Account for Energy Losses by Macro-Roughness Elements in Modeling Tsunami Inundation

Coastal Structures 2019 - Nils Goseberg, Torsten Schlurmann (eds) - © 2019 Bundesanstalt für Wasserbau
ISBN 978-3-939230-64-9 (Online) - DOI: 10.18451/978-3-939230-64-9_056

Source Term Formulae to Account for Energy Losses by Macro-Roughness Elements in Modeling Tsunami Inundation

S. Leschka
DHI WASY GmbH, Bremen, Germany
H. Oumeraci
TU Braunschweig, Germany (retired)

Abstract: Dam break and tsunami bore propagation and inundation are commonly simulated using large-scale depth-averaged models, e.g. based on non-linear shallow water (NLSW) equations. In such models, the quadratic friction law with a selected Manning's coefficient is generally applied to account for the effect of the bottom surface roughness in each computational cell. Macro-roughness elements (MRE) such as buildings and tree vegetation generally represent a part of coastal areas. Using purely empirical Manning's coefficients to account for such large objects is not physically sound and might result in large uncertainties. To better understand the effects of relevant parameters such as shape, size and arrangement of the MREs on tsunami bore propagation and inundation, an extensive parameter study is performed, using a systematically validated three-dimensional CFD model (OpenFOAM®). The tsunami bore-like flow conditions are obtained using an initial impoundment dam break. The results are analysed with regard to different flow regimes of tsunami inundation: (i) an unsteady phase during the arrival of the bore and (ii) a quasi-steady phase, when the maximum flow depth occurs. The impact of each of five varied MRE parameters is determined. The analysis reveals that the volume flux is predominantly reduced at the first MRE row. During the unsteady phase, the relative spacing S_G/D_B has the greatest impact on the volume flux, while the relative height h_B/h_{max} dominates during the quasi-steady phase. Inside the MRE zone, the effect of the arrangement on the reduction of the volume flux dominates during both unsteady and quasi-steady phases of the bore propagation. Multi-regression analysis of the numerically generated data resulted in the formulation of the source terms S_{MRE} (for drag and inertia) as a function of the most relevant MRE parameters and flow characteristics. The new source terms are implemented in the NLSW model COMCOT (Wang & Liu, 2011). The model performance with and without the implemented new source term are then comparatively applied to reproduce the inundation experiments in the laboratory (Park et al. 2013).

Keywords: tsunami hydrodynamics, coastal flooding, macro-roughness elements, numerical coastal modelling, CFD OpenFOAM, NLSW code COMCOT

1 Introduction

Tsunami propagation and inundation are commonly simulated using large-scale depth-averaged models. In such models, the quadratic friction law with a selected Manning's coefficient is generally applied to account for the effect of bottom surface roughness in each computational element. Buildings and tree vegetation in coastal areas are usually smaller than the computational element size. Using empirical Manning's coefficients to account for such large objects is not physically sound and, particularly in tsunami inundation modelling, this may result in large uncertainties. Therefore, an improved understanding of the processes associated with the hydraulic resistance of the so-called macro-roughness elements (MRE) is required. Relevant parameters such as shape, height and arrangement of the MRE are investigated through numerical tests using a validated three-dimensional CFD model. Given the correlation of such parameters to the MRE-induced hydraulic resistance,

empirical formulae are developed and directly implemented as sink terms in depth-averaged numerical solvers such as non-linear shallow-water (NLSW) models.

In the last decades, various efforts have been deployed to improve the understanding of the effects of MRE on flow and inundation processes such as Arnason (2004), Goseberg (2013), Husrin (2013), Bonakdar (2014), Yeh et al. (2014), Maza et al. (2015); Younis et al. (2016), Sridhar (2019). Approaches for considering MRE in urban flooding have been developed for example by Soares-Frazao & Zech (2008), Gayer et al. (2010), Muhari et al. (2011), Cassan et al. (2017).

In this paper, the methodology to determine the source terms due to MRE is described in section 2. The source term is developed in section 3 and is compared with laboratory experiments of Park et al., (2013) in section 4.

2 Methodology

An OpenFOAM® based 3D two-phase Reynolds-averaged Navier-Stokes (RANS) model including the volume of fluid (VOF) method is validated against data sets from five different laboratory experiments (Leschka et al., 2014). The performance of the 3D-CFD models are evaluated by means of non-dimensional statistical criteria for time series comparisons. A numerical test program with more than 20 simulations is developed, including the variation of the shape, arrangement, density and relative height of the MRE. The propagation of the bore is analyzed mainly based on the water content of a computational cell and flow velocity u. They are spatially and temporally integrated over the cross-section of each of the three segments along the MRE zone in Figure 1 to obtain volume flux p(x) and flow depth h, which represent flow parameters typical in NLSW equations. Figure 2 illustrates the procedure to derive the source terms.

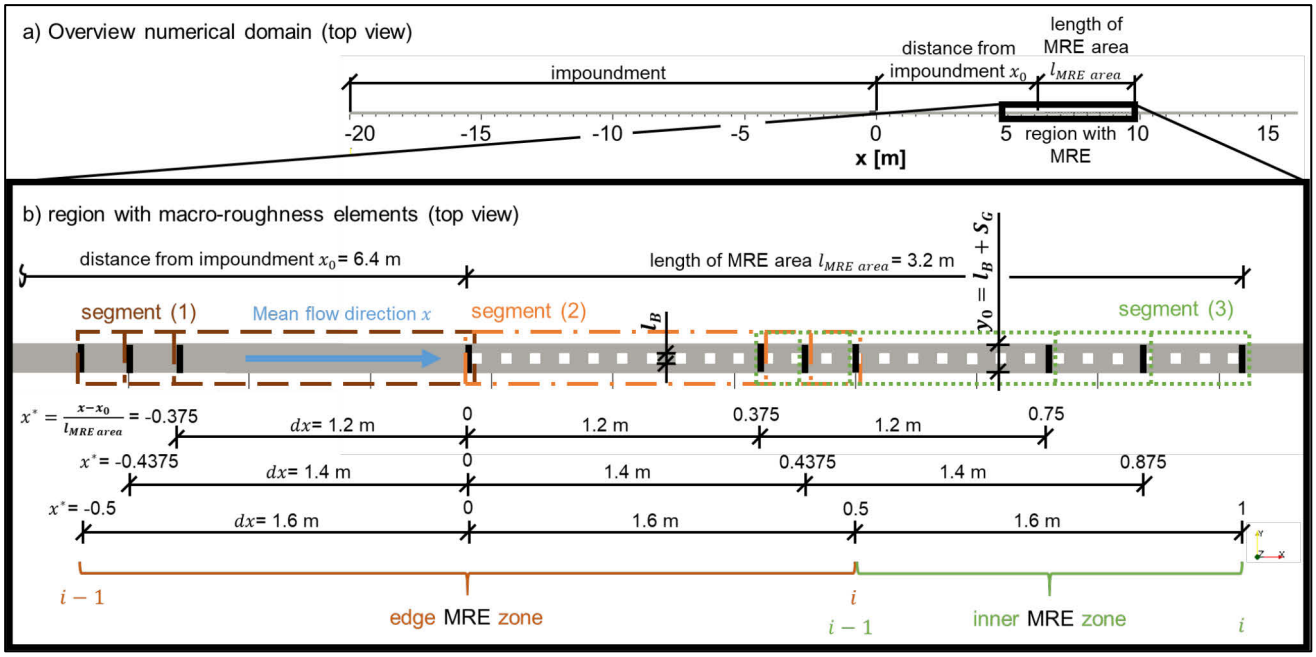

Fig. 1. Selected cross sections in the edge zone and the inner zone of the area of macro-roughness elements (MRE): a) Overview of numerical domain, b) area of MRE. Segments 1 (dashed) and 2 (dash-dotted) form the edge zone and the segment 3 (dotted) is the inner zone of MRE. The vertical black bars indicate the selected cross-sections & the squares indicate the MRE.

The data obtained from the validated CFD model is used to calculate the source term for (i) the reference case without MRE, where only friction losses can be observed, and (ii) the cases with MRE (respectively Steps 1 and 2 in Fig. 2). The difference between the results of the reference case (S_{fx}) and the results of the cases with MRE (S_{total}) represents the sink term S_{MRE} associated with the MRE-induced energy losses due to form drag, inertia and increased turbulence (Step 3 in Fig. 2). It can be calculated using

$$\frac{\partial p(x)}{\partial t} + \frac{\partial}{\partial x}\left(\frac{p(x)^2}{h} + gh^2 - \frac{h}{\rho}\tau_{xx}\right) = ghS_{fx} + S_{MRE} = S_{total} \quad (1)$$

where p(x) is the volume flux in the direction of x, t is the time, h is the flow depth, g is the acceleration due to gravity, ρ is the density of the fluid and τ_{xx} is the turbulent shear stress. S_{fx} describes the friction losses due to bottom surface roughness, S_{MRE} represents the source term, which is related to the modifications of the arrangement angle Ψ, the shape (by means of drag coefficient C_D), the height h_B and the width D_B of the MRE. The flow and MRE parameters are defined in Fig. 3.

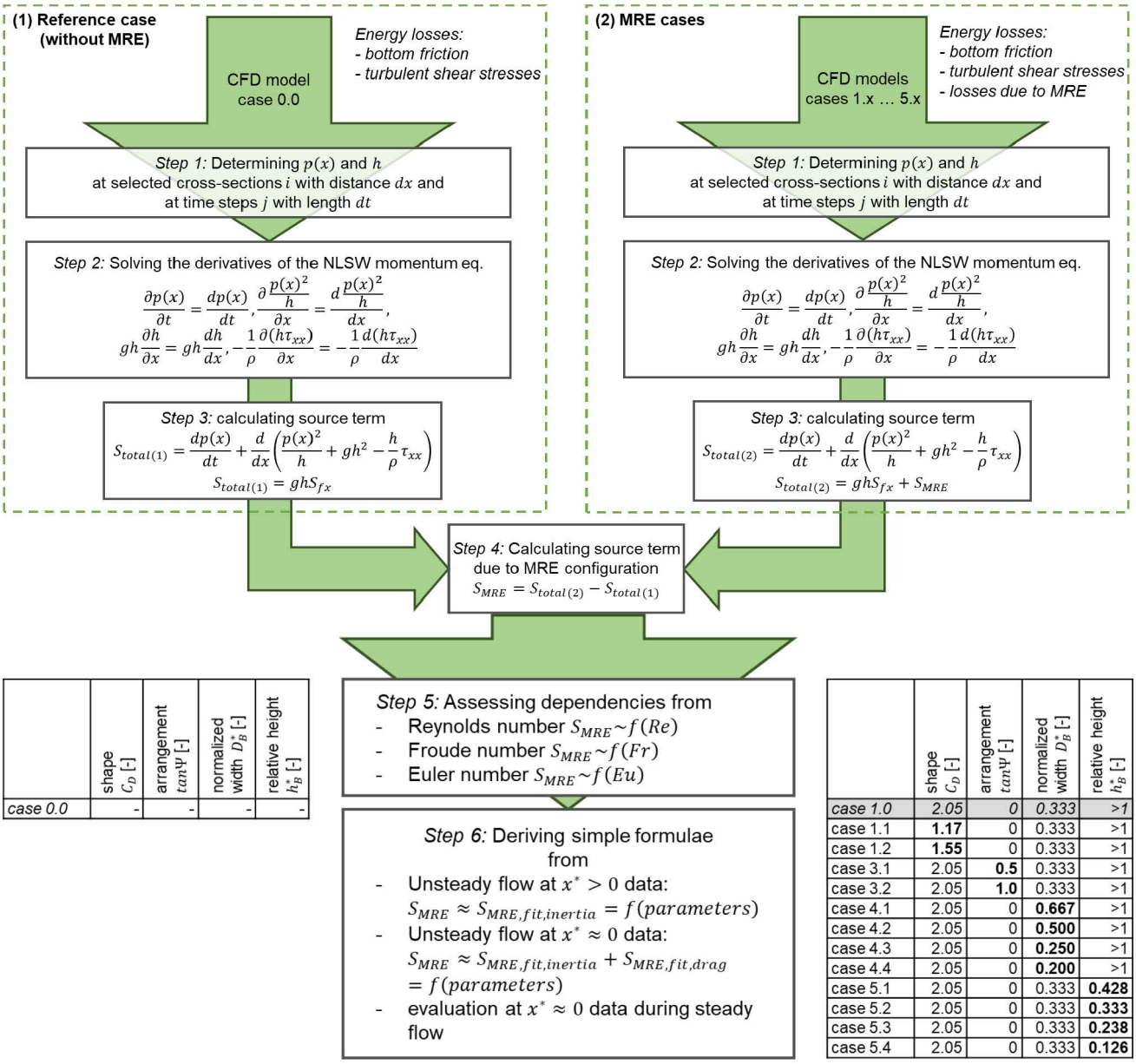

	shape C_D [-]	arrangement $tan\Psi$ [-]	normalized width D_B^* [-]	relative height h_B^* [-]
case 0.0	-	-	-	-

	shape C_D [-]	arrangement $tan\Psi$ [-]	normalized width D_B^* [-]	relative height h_B^* [-]
case 1.0	2.05	0	0.333	>1
case 1.1	**1.17**	0	0.333	>1
case 1.2	**1.55**	0	0.333	>1
case 3.1	2.05	**0.5**	0.333	>1
case 3.2	2.05	**1.0**	0.333	>1
case 4.1	2.05	0	**0.667**	>1
case 4.2	2.05	0	**0.500**	>1
case 4.3	2.05	0	**0.250**	>1
case 4.4	2.05	0	**0.200**	>1
case 5.1	2.05	0	0.333	**0.428**
case 5.2	2.05	0	0.333	**0.333**
case 5.3	2.05	0	0.333	**0.238**
case 5.4	2.05	0	0.333	**0.126**

Fig. 2. Flow chart of the analysis procedure to derive the source term S_{MRE} describing the energy losses due to macro-roughness elements (MRE) from the data obtained from CFD modelling, which are summarized in the included tables.

All parameters represent averaged values and are valid for the entire unit area dxdy, where dx and dy are the unit length and unit width, respectively. S_G is the spacing between the MRE, D_B is the width of the MRE and h_B is the height of the MRE. Only the part of the MRE is taken into account, which is subject to the flow and referred to as effective height of the MRE

$$h_{B,eff} = min\left(h_{eff}, h_B\right) \tag{2}$$

with the effective flow depth

$$h_{eff} = f_{eff}h \tag{3}$$

which is larger than flow depth h. This is expressed by a factor f_{eff}=2 (determined during the parameter study, not shown here), because it can be expected that, for instance, due to the run-up of the bore on a front face of a MRE, also MRE parts located above the (spatially averaged) water

surface may contribute to the energy losses. In equation (3), h is determined as the average of the flow depth at the upstream and the downstream cross-section i-1 and i

$$h^*_{B,eff} = \frac{h_{B,eff}}{h} = \frac{min(h_{eff},h_B)}{h} \tag{4}$$

The width of the MRE D_B in Fig. 3 is normalized by the sum of MRE width and spacing (D_B+S_G). The normalized width, which might represent a blockage ratio of the flow, reads

$$D^*_B = \frac{D_B}{D_B+S_G} \tag{5}$$

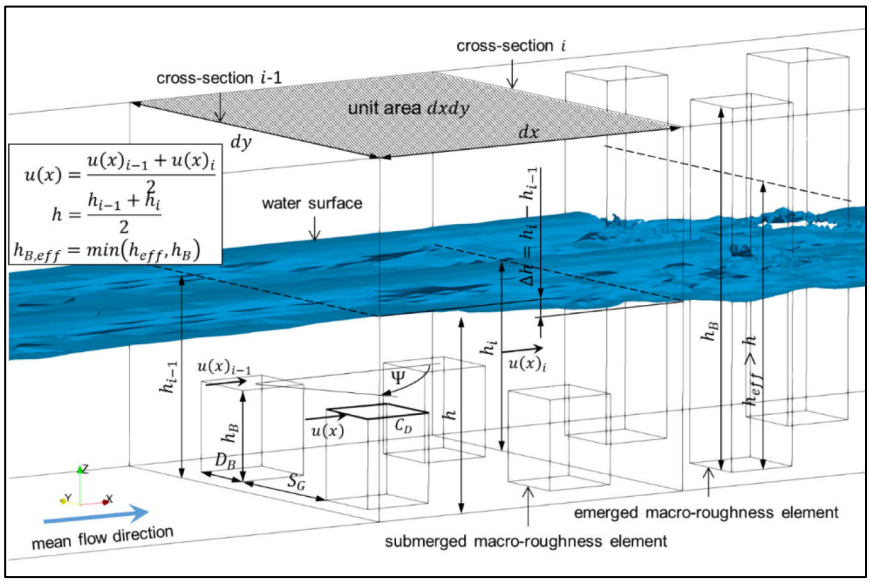

Fig. 3. Definition of flow and macro-roughness parameters for both emergent and submerged MRE.

The arrangement angle Ψ in Figure 3 is defined as the angle between the mean flow direction and the orientation of the group of MRE.

By subtracting the solution of the reference case without MRE $S_{total(1)}$ from the solution of the MRE cases $S_{total(2)}$, the solution of the source term SMRE is obtained (Step 4 in Fig. 2).

Dimensional analyses are performed to determine correlations of the sink term with the Reynolds number, Froude number and Euler number (Step 5 in Fig. 2).

By means of these quantities, multi-regression analyses are performed, and "empirical" relationships are obtained (Step 6 in Fig. 2), which describe the effect of the MRE arrangement, their height, the distance between them and their shape on the sink term S_{MRE}.

3 New formulae for the source terms

Based on the dimensional analysis, the source terms S_{MRE} obtained during the steady and the unsteady phase of bore propagation at the upstream edge and inner zone of MRE (see Fig. 1) are related to the Reynolds number Re, Froude number Fr and Euler number Eu.

Froude number Fr (flow inertia to gravity ratio) can be used to assess the unsteady phase of bore propagation. Inertia is interpreted as a variation of the flow velocity over time.

Reynolds number Re (drag force to viscous force ratio) is associated with drag and can be used to describe the steady phase of bore propagation.

Euler number Eu (ratio of pressure gradient to variation of flow velocity over space) is related to dynamic pressure differences, which occur between the upstream faces of the MRE, where the flow is slowed down, and beside the MRE near the lateral faces, where high flow velocities occur.

Figure 4 shows the velocity fields around cubic, cylindrical and diamond-shaped MREs. High velocity gradients are mainly observed in the edge zone of the MRE. Such velocity gradients can be expected during steady and unsteady flow conditions. It is noted that they occur inside the unit areas dxdy on sub-grid scale and are not captured by the cross-sections in which the flow parameters are calculated. Therefore, it is difficult to use Eu in the source term S_{MRE}. However, here, drag consists

predominantly of form drag, which dominates over friction drag in high Re flow (which is here the case). Form drag results from the pressure distribution over the MRE. Therefore, the pressure force can be set equal to the drag force

$$F_{drag} = \frac{1}{2}\rho C_D A_B \left(\frac{p(x)}{h}\right)^2 = Eu \cdot u^2 l_0^2 \rho = F_{pressure} \quad (6)$$

If further the characteristic length l_0 is expressed as

$$l_0 = \sqrt{A_B} = \sqrt{D_B . min(h, h_B)} \quad (7)$$

with the front face area A_B as a product of the MRE width D_B and the submerged part of the MRE height h_B, then it can be shown that $Eu=1/2C_D$. So, as long as C_D is part of the solution, Eu is implicitly accounted for and does not need to be explicitly considered in the further analysis.

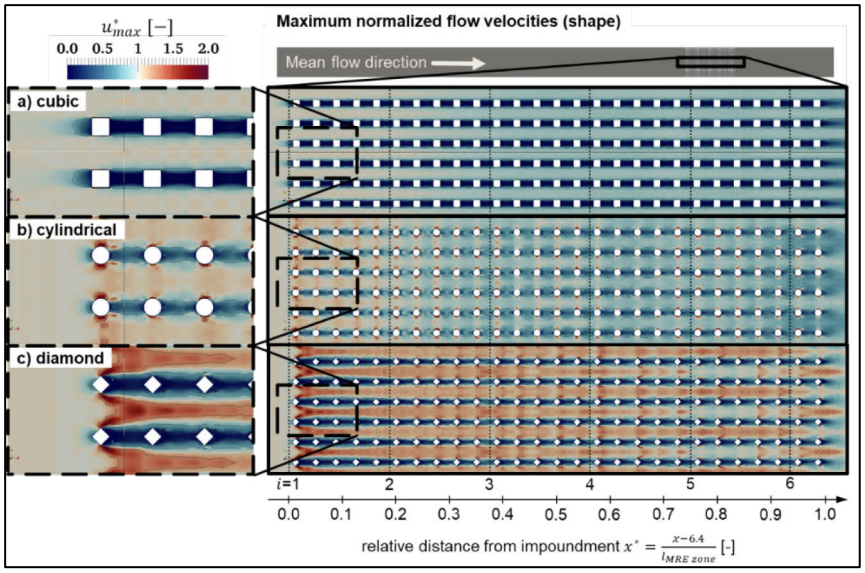

Fig. 4. Normalized maximum flow velocities $u_{max}^* = u_{(case1.x,max)}/u_{(0.0,max)}$ in mean flow direction z= 0.05 m above the bottom through a) cubic , b) cylindrical and c) diamond-shaped macro-roughness elements with a relative distance of S_G/D_B = 2.0. The black contour lines indicate the boundaries at which maximum flow velocities are by 25 % higher or lower compared to the reference case for the same inflow conditions without any macro-roughness elements. The dotted lines symbolize the segment i.

3.1 Inertia during the unsteady phase of bore propagation in the inner MRE zone

The dependency between S_{MRE} and the Froude number Fr is shown in Figure 5.
The data in Fig. 5 shows a clear dependency of the source term S_{MRE} from the Froude number Fr and can be expressed as S_{MRE}=f(Fr).

The shape variations (expressed by drag coefficient C_D) are not directly related to S_{MRE}. For proportionality , Fr for the case with C_D= 2.05 (case 1.0) should be smaller than for case 1.2 with C_D= 1.55 (case 1.2). For an explanation, it is to note that inside the MRE zone, the flow velocities vary largely over a cross-section (which is also indicated in Fig. 4) and that the MRE are located in slow flow regions. It is seen that even if the averaged flow velocities in the cross-sections are similar, the flow approaching the front face(s) of an individual MRE inside the cross-section vary considerably, is much smaller in case of cubic MRE than in case of diamond-shaped or cylindrical MRE (case 1.1). Therefore, the here used averaged flow velocity used in Froude number Fr cannot lead to a direct relation of C_D with S_{MRE}. Because the energy losses with S_{MRE}<0.1 m²/s² are very small, which is approximately the range of uncertainty of 2·STDEV= 0.07 m²/s² (not shown), the influence of the shape on S_{MRE} is neglected here.

Regarding the normalized height h_B^* variations, it is noted that the submerged cases with a minimum h_B^* = 0.442 (case 5.4, see Fig. 5) lead to slightly higher energy losses than the fully emerged case 1.0, because additional flow disturbance can be induced downstream of the MRE, when the MRE is overflown. It is further noted, that the cases 5.1 and 5.2 appear to be emerged during the investigated conditions for the averaged flow depth h= 0.118 m and h= 0.112 m, respectively.

Therefore, one would expect similar energy losses as for the fully emerged case 1.0, but both cases show higher energy losses than case 1.0. This is because the MRE are overflown in cases 5.1 and 5.2.

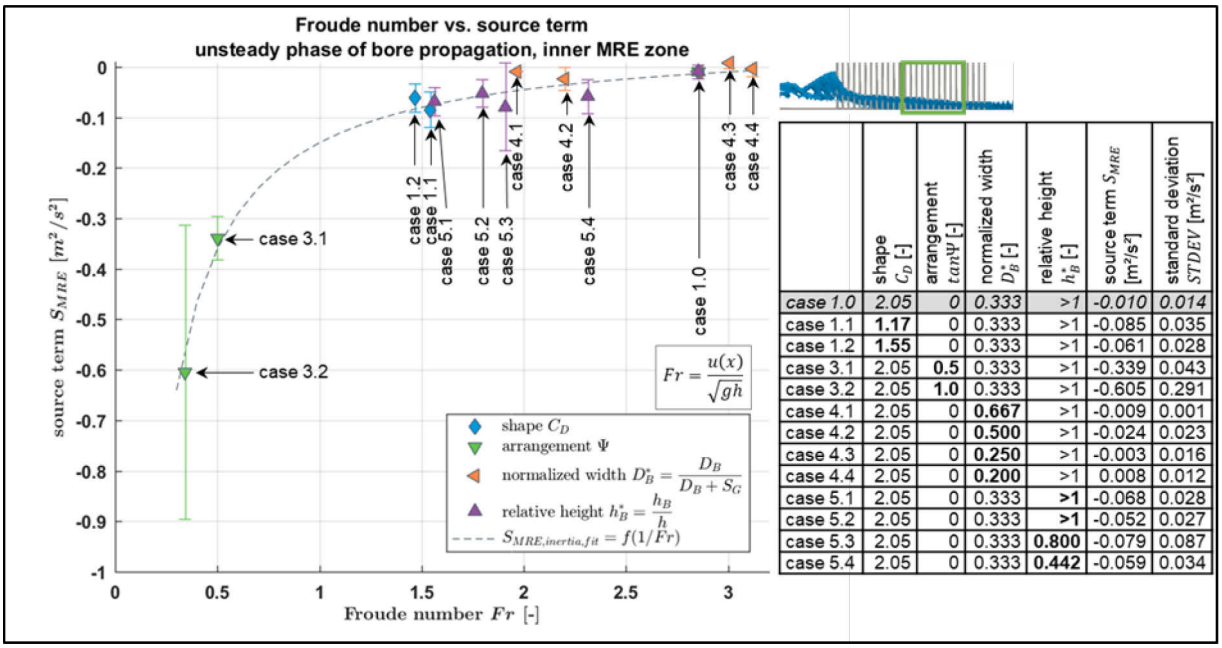

	shape C_D [-]	arrangement $tan\Psi$ [-]	normalized width D_B^* [-]	relative height h_B^* [-]	source term S_{MRE} [m²/s²]	standard deviation $STDEV$ [m²/s²]
case 1.0	*2.05*	*0*	*0.333*	*>1*	*-0.010*	*0.014*
case 1.1	**1.17**	0	0.333	>1	-0.085	0.035
case 1.2	**1.55**	0	0.333	>1	-0.061	0.028
case 3.1	2.05	**0.5**	0.333	>1	-0.339	0.043
case 3.2	2.05	**1.0**	0.333	>1	-0.605	0.291
case 4.1	2.05	0	**0.667**	>1	-0.009	0.001
case 4.2	2.05	0	**0.500**	>1	-0.024	0.023
case 4.3	2.05	0	**0.250**	>1	-0.003	0.016
case 4.4	2.05	0	**0.200**	>1	0.008	0.012
case 5.1	2.05	0	0.333	**>1**	-0.068	0.028
case 5.2	2.05	0	0.333	**>1**	-0.052	0.027
case 5.3	2.05	0	0.333	**0.800**	-0.079	0.087
case 5.4	2.05	0	0.333	**0.442**	-0.059	0.034

Fig. 5. Source terms S_{MRE} vs. Froude number Fr during unsteady conditions in the inner zone for different unit lengths dx (For the definition of the MRE parameters see Fig. 3). The error bars indicate the standard deviations.

Regarding the normalized width D_B^* variations, the lowest value of D_B^*= 0.2 (case 4.4) is not associated with the lowest value of S_{MRE}, and the largest value of D_B^*= 0.667 (case 4.1) is not associated with the largest value of S_{MRE}, as would be expected. The reason for the observed inconsistencies lies mainly in the presence of the MRE near the cross-sections, because the MRE influence the local flow velocities and flow depths, which can may have a high significant effect on the averaged flow parameters at the cross-sections.

The variation of the arrangement angle Ψ causes energy losses of S_{MRE}> 0.3 m²/s², which are proportional to arrangement angle Ψ which is by far the most important parameter to describe the energy losses in the inner MRE zone during the unsteady phase of the bore propagation.

3.2 Drag during the steady phase of bore propagation in the edge MRE zone

The dependency between the source term during steady phase of bore propagation in the edge MRE zone S_{MRE} and the $Re(l_0)$ is depicted in Figure 6.

By visual inspection of Fig. 6, clear dependencies of the energy losses S_{MRE} from $Re(l_0)$ can be identified. It seems that for the variations of relative height h_B^* and arrangement angle Ψ, the dependency of S_{MRE} from Re can be expressed as S_{MRE} (h_B^*,Ψ)~f(Re), while for the variation of the normalized width D_B^*, the dependency is rather S_{MRE} (D_B^*)~f($1/Re^x$). When investigating individual parameter variations further, the following observations are made.

The normalized width D_B^* clearly appears to have the greatest influence on the energy losses S_{MRE}.

Regarding the arrangement angle Ψ, it is noted that increasing Ψ leads to a reduction of S_{MRE}, which is the opposite from the behavior observed in the inner MRE zone. It becomes clear that the most upstream MRE row in the edge zone becomes more permeable if Ψ>0, which leads to smaller energy losses compared to the arrangement, in which Ψ= 0°.

Regarding the shape variations (expressed by drag coefficient C_D), no clear dependency is seen between energy losses S_{MRE} and Reynolds number Re. On one hand, case 1.0 using C_D= 2.05 (cubic shape) leads to the greatest S_{MRE}. Case 1.1 with C_D=1.17 (cylindrical shape) leads to greater S_{MRE} than case 1.2 with C_D=1.55 (diamond-shaped), so that S_{MRE} is not proportional to C_D. On the other hand, Re is considerably higher in case 1.1 than in case 1.2, for which Re is slightly higher than in case 1.0, so that Re~C_D. This is in agreement with the observation Fig. 4, where it is noted that in case 1.2 the flow is more deflected by the front faces of the diamond than blocked, allowing for higher (averaged) flow velocities between the MRE, but also considerably smaller flow velocities at the front faces of the diamond-shaped MRE, resulting in smaller S_{MRE}. This explains why the energy losses in the cases

1.2 (C_D=1.55) S_{MRE}= -0.123 m²/s² can be slightly smaller than in the case 1.2 (C_D=1.17) S_{MRE}=-0.136 m²/s². However, it needs to be mentioned that the standard deviations (STDEV) due to local flow effects in case 1.2 (C_D= 1.55) and case 1.1 (C_D= 1.17) take high values of STDEV= 0.117 m²/s² and STDEV= 0.076 m²/s², respectively, compared to the difference between the calculated energy losses between both cases 1.1 and 1. 2, $\Delta S_{MRE}=|S_{MRE,case1.1}-S_{MRE,case1.2}|$= 0.013 m²/s, which imposes high uncertainty on any quantitative conclusion.

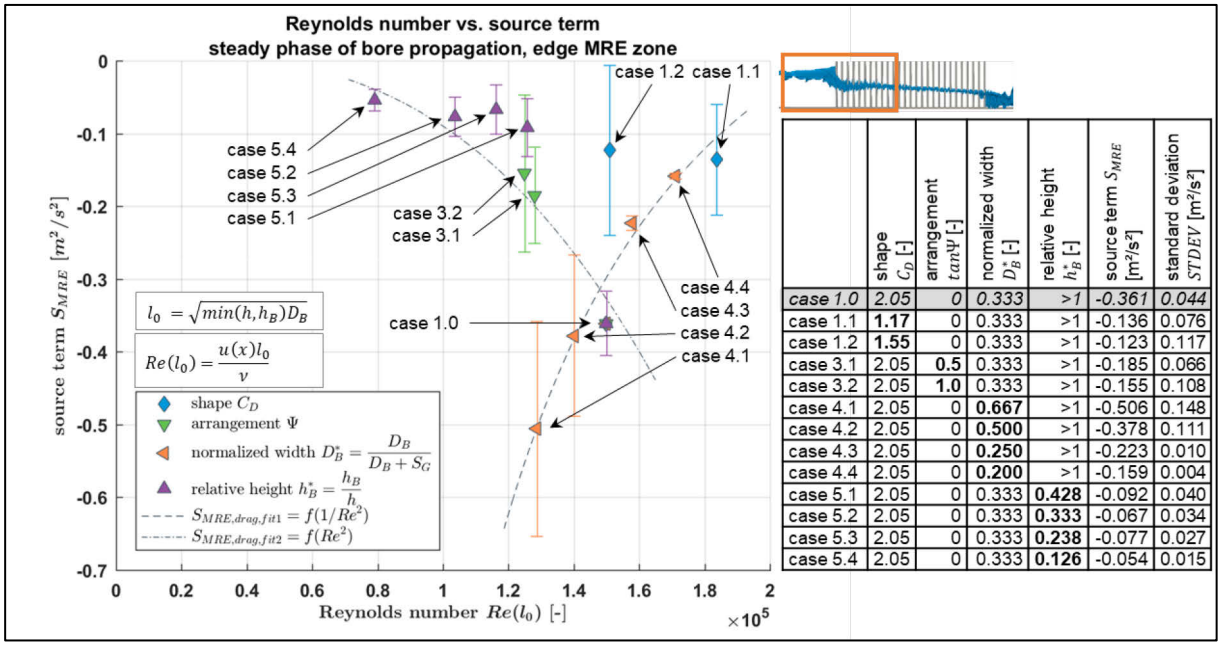

	shape C_D [-]	arrangement $tan\Psi$ [-]	normalized width D_B^* [-]	relative height h_B^* [-]	source term S_{MRE} [m²/s²]	standard deviation $STDEV$ [m²/s²]
case 1.0	*2.05*	*0*	*0.333*	*>1*	*-0.361*	*0.044*
case 1.1	**1.17**	0	0.333	>1	-0.136	0.076
case 1.2	**1.55**	0	0.333	>1	-0.123	0.117
case 3.1	2.05	**0.5**	0.333	>1	-0.185	0.066
case 3.2	2.05	**1.0**	0.333	>1	-0.155	0.108
case 4.1	2.05	0	**0.667**	>1	-0.506	0.148
case 4.2	2.05	0	**0.500**	>1	-0.378	0.111
case 4.3	2.05	0	**0.250**	>1	-0.223	0.010
case 4.4	2.05	0	**0.200**	>1	-0.159	0.004
case 5.1	2.05	0	0.333	**0.428**	-0.092	0.040
case 5.2	2.05	0	0.333	**0.333**	-0.067	0.034
case 5.3	2.05	0	0.333	**0.238**	-0.077	0.027
case 5.4	2.05	0	0.333	**0.126**	-0.054	0.015

Fig. 6. Source terms S_{MRE} vs. Reynolds number Re during steady conditions in the upstream edge MRE zone for different dx (For the definition of the MRE parameters see Fig. 3). The error bars indicate the standard deviations.

Regarding the relative height h_B^* variations in the cases 5.2 and 5.3, in which respectively with h_B^*= 0.238 and h_B^*= 0.333, respectively, an inconsistency is seen as the energy S_{MRE} losses seem to increase with increasing Re, which (i) is opposite to what one would expect and (ii) is also opposite to the tendency noted for the cases 5.1 and 5.4, where S_{MRE} decreases with increasing Re. This observation might be due to local flow effects as discussed in section 3.1, because the absolute difference between the mean energy losses in cases 5.2 and 5.3, $\Delta S_{MRE}=|S_{MRE,case5.2}-S_{MRE,case5.3}|$= 0.01 m²/s² is smaller than the standard deviation STDEV= 0.033 m²/s² (see Fig. 6). The energy losses for the cases with h_B^*<0.5 take values of S_{MRE}< 0.1 m²/s², only.

3.3 Deriving simple formulae for the source terms due to drag and inertia

The source term is developed in analogy to the Morison equation (Morison, et al., 1950)

$$S_{MRE,fit} = S_{MRE,fit,inertia} + S_{MRE,fit,drag} \tag{9.a}$$

$S_{MRE,fit,inertia}$ and $S_{MRE,fit,drag}$ are developed independently from each other, each by sequential fitting of the CFD data obtained from each parameter variation. $S_{MRE,fit,drag}$ is only applied in the edge MRE zone due to the factor $\partial D_B^*/\partial x$, which is zero in the inner MRE zone. Therefore, $S_{MRE,fit,inertia}$ is developed first in the inner MRE zone during the unsteady phase of bore propagation. The edge MRE zone is then considered to estimate the drag contribution $S_{MRE,fit,drag}$, to the total term $S_{MRE,fit}$.
The source term due to inertia and the source term due to drag in the upstream edge MRE zone read

$$S_{MRE,fit,inertia} = \frac{\partial p(x)}{\partial t}\frac{\sqrt{gh}}{\frac{p(x)}{h}}[1.3 - cos(4\Psi)]^{0.33} \tag{9.b}$$

$$S_{MRE,fit,drag} = -0.4\frac{\partial D_B^*}{\partial x}\frac{p(x)^2}{h}h_{B,eff}^* C_D[0.7 + 0.3cos(4\Psi)]^{0.1} \tag{9.c}$$

in which the relative effective height is defined as $h_{B,eff}^{*}$=min(2h,h_B)/h, taking into account that, due to flow depth variations in a unit area and due to runup on the front faces of the MRE, higher parts of the MRE of up to twice the flow depth may contribute to the energy losses.

Scatter analyses (not shown here) indicate that energy losses in the inner MRE zone depend on the arrangement angle Ψ, while all other parameters lead to very small energy losses (see also Fig. 5). In the upstream edge MRE zone, the energy losses depend on all four MRE parameters. They are underestimated by up to -20 % due to the variation of Ψ. When applying the source terms to steady flow conditions in the upstream edge MRE zone, the fit tends to underestimate energy losses derived from the CFD parameter tests by up to -45%, mainly due to the application of the drag coefficient C_D, which is used as constant value for all flow conditions.

4 Application of the new formulae in COMCOT

The derived formulae (Eqs 9a & 9b) are implemented into the NLSW model COMCOT (Wang & Liu, 2011). The code is then applied to the laboratory experiments on tsunami inundation through the urban area of the town of Seaside, Oregon, which were performed in a scale of 1:50 (Rueben et al., 2011). For details on the experiments see the latter reference.

For reasons of simplification, it is not distinguished between the blocking of the flow in x or in y direction. Instead, unidirectionality of D_B^{*} is assumed so that it can easily be obtained from high resolution geodata in real scale applications, which allows for deriving the fraction of areas occupied by buildings A_B^{*}. Then,

$$D_B^* = \sqrt{A_B^*} \text{ with } A_B^* = min\left(\frac{A_B}{dxdy}, 1\right) \tag{10}$$

Compared to traditional approaches using Manning's coefficient n, here, four additional layers are to be prepared. An example for such layers in the onshore section for a grid resolution dx=10m (0.2m in model scale), which is too coarse to represent individual buildings in the bathymetry, are presented in Figure 7.

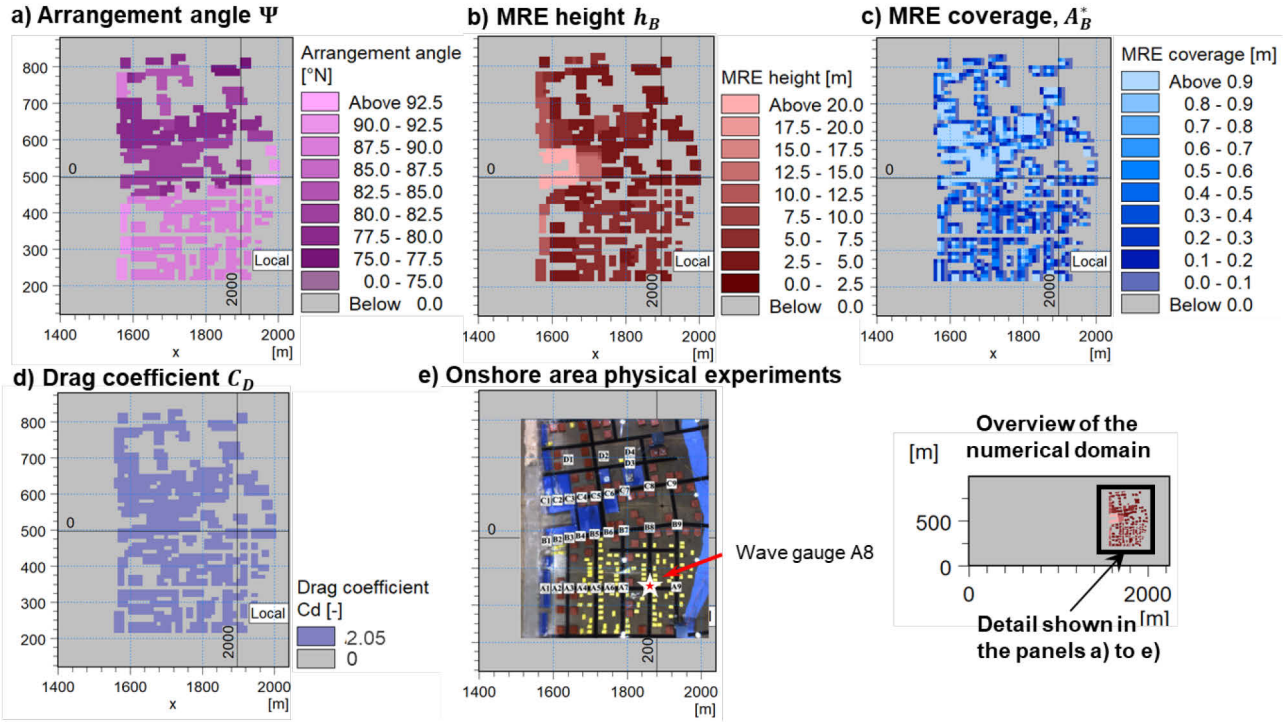

Fig. 7. Input layers for MRE model: a) arrangement angle Ψ, b) MRE height h_B, c) MRE coverage A_B^{*}, d) MRE shape (Drag coefficient C_D), e) Onshore area of the physical experiments (modified from Rueben, et al., 2011).

Due to spatial limitations of the experiments, the maximum inundation area could not be obtained. Therefore, the moment of arrival of the tsunami bore at wave gauge A8 is used as reference inundation. Figure 8 presents the inundation areas of various roughness approaches. The results are summarized in Table 1.

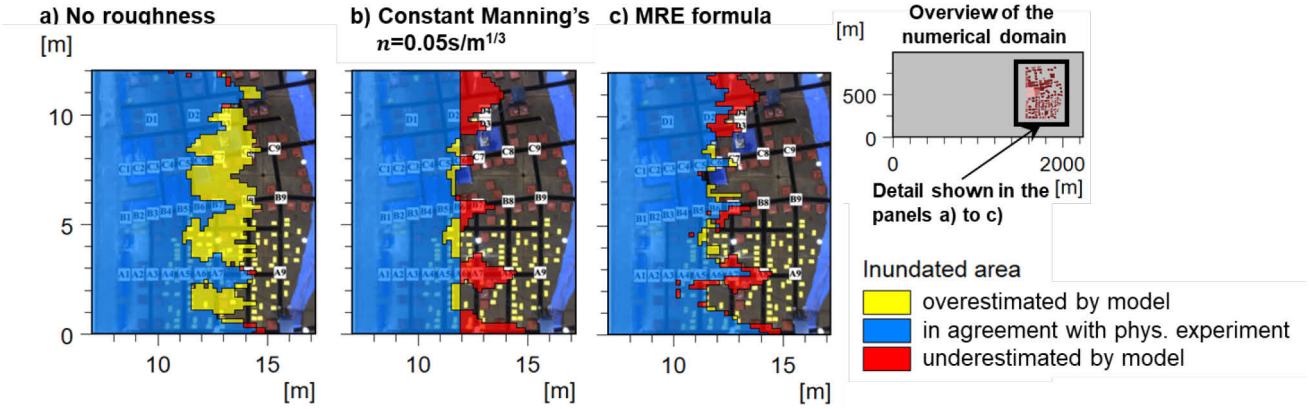

Fig. 8. Inundated areas after t=28.85s (arrival at wave gauge A8): a) no roughness consideration, b) constant Manning's n=0.05s/m$^{1/3}$, c) MRE formulae (eqs 9a & 9b).

Tab. 1. Result summary for the application of the new formulae (eqs 9a & 9b) in COMCOT to reproduce laboratory experiments

Model	Underestimated inundation area A_U [m²]	Area of agreement between experiment and model A_A [m²]	Overestimated inundation area A_O [m²]	Deviation of model from experiment $PR=(A_U+A_O)/A_C$ [-]
No roughness	0.80	67.92	18.64	0.286
Constant n	7.20	58.80	2.12	0.205
MRE formulae	9.92	61.52	1.68	0.144

It can be noted that the model without any roughness consideration, the inundated area is considerably overestimated, while in case of the constant Manning's value n and the MRE formula, the overestimated areas are about an order of magnitude smaller. In turn, the no roughness model underestimate very slightly regions which are inundated during the physical experiments. The underestimation in both other models is moderate. A measure for the agreement of the modelled with physical inundation is defined as the performance ratio

$$PR = \frac{A_U + A_O}{A_A} \tag{11}$$

between the sum of the underestimated area A_U and overestimated area A_O and the inundated area in which the model agrees with the physical experiment A_A. Smaller values indicate higher agreement with the physical experiments. The MRE formula leads to the highest agreement among the tested methods.

5 Summary und concluding remarks

Source terms S_{MRE} for the drag and inertia contributions to energy losses due to macro-roughness elements (MRE) are developed which can be introduced in non-linear shallow water models or in any other depth-averaged large-scale model. The MRE are parametrized by their arrangement angle, height, width, spacing and shape (expressed by drag coefficient C_D).

From the results of a systematic parameter study using a well-validated CFD model, clear dependencies of the source terms S_{MRE} from the Froude number Fr in the inner MRE zone during the unsteady phase of bore propagation are observed, but only the variation of the arrangement angle Ψ leads to considerably large energy losses. Furthermore, clear dependencies from the Reynolds number Re are observed in the upstream edge MRE zone during the steady phase of bore propagation for the normalized MRE width D_B^*, the relative height h_B^* and Ψ, while the drag coefficient C_D (describing the shape of the MRE) cannot be related to S_{MRE}. C_D does not account for effects such as deflection of flow towards the downstream-located MRE. In case of diamond-shaped MRE, deflection results in hindering flow velocities between the MRE and in very low flow velocities upstream of the MRE, leading to relatively small energy losses, so that no clear correlation is observed between S_{MRE} and C_D.

The fitted source term $S_{MRE,fit}$ indicates a very good agreement during the unsteady phase of bore propagation at the bore front, while the energy losses during the quasi-steady current during the later phases of bore propagation are underestimated.

The results suggest that using a constant drag coefficient cannot represent the energy losses equally well during both steady and unsteady flow phases. Further research is required to assess the impact of flow deflection towards neighbouring MRE to consider the variation of flow velocities within a cross-section as induced by upstream MRE. This might result in the development of an alternative form factor, which accounts for deflection and is therefore more appropriate to describe the shape effect of MRE in a group.

Local flow effects due to the presence of the MRE "pollute" the results when determining the spatial derivatives between the cross-sections inside the MRE zone. Instead of analyzing and averaging the variables flow depth h(x) and volume flux p(x) at the cross-sections only, it might be more appropriate to average the flow conditions throughout the water column over in the entire unit area dxdy.

The developed formulae for the source term S_{MRE} are implemented in the NLSW code COMCOT (Wang & Liu, 2011). First comparisons with laboratory experiments show a relatedly good ability of these formulae to reproduce the inundated area. Further applications, including benchmark tests in real scale (e.g. Jakeman, et al., 2010), should be performed for a more detailed evaluation.

References

Arnason, H. (2004): "Interactions between an Incident Bore and a Free-Standing Coastal Structure" PhD thesis, University of Washington.

Bonakdar, L. (2014): "Pile Group Effect on the Wave Loading and Pile Group Supported Offshore Structures-A Large Scale Model Study" PhD Thesis, TU Braunschweig, Germany.

Bricker, J.D., Gibson, S., Takagi, H., Imamura, F. (2015): "On the Need for Larger Manning's Roughness Coefficients in Depth-Integrated Tsunami Inundation Models" Coastal Engineering Journal (JSCE), 57(2).

Cassan, L., Roux, H., Garambois, P.-A. (2017): "A Semi-Analytical Model for the Hydraulic Resistance Due to Macro-Roughnesses of Varying Shapes and Desities" Water, 9, 637.

Goseberg, N. (2013): "Reduction of maximum tsunami run-up due to the interaction with beachfront development-application of single sinusoidal waves" Nat. Hazards Earth Syst. Sci., 13, 2991-3010.

Husrin, S. (2013): "Attenuation of Solitary Waves and Wave Trains by Coastal Forests" PhD Thesis, TU Braunschweig, Germany, University of Florence, Italy.

Jakeman, J.D., Nielsen, O.M., van Putten, K., Mleczko, R., Burbidge, D., Horspool, N. (2010): "Towards spatially distributed quantitative assessment of tsunami inundation models" Ocean Dynamics, 60(5), 1115-1138.

Leschka, S., Oumeraci, H., Larsen, O. (2014): "Hydrodynamic Forces on a Group of Three Emerged Cylinders by Solitary Waves and Bores: The Effect of Cylinder Arrangement and Distances", Journal of Earthquake and Tsunami, World Scientific, vol. 8 (3), 144005 (36 pages)

Maza, M., Lara, J.L., Losada, I.J., Ondiviela, B., Trinogga, J., Bouma, T.J. (2015): "Large-scale 3D experiments of wave and current interaction with real vegetation. Part 2: Experimental analysis" Coastal Engineering, 106, 73-86.

Morison, J.R., O'Brien, M.P., Johnson, J.W., Schaaf, S.A. (1950): "The force exerted by surface waves on piles" Petroleum Transactions, 189, 149-154.

Muhari, A., Imamura, F., Koshima, S., Post, J. (2011): Examination of three practical run-up models for assessing tsunami impact on highly populated areas" Nat. Hazards Earth Syst Sci, 11, 3107-3123.

Park, H., Cox, D.T., Lynett, P.J., Wiebe, D.M. and Shin, S., 2013. Tsunami inundation modeling in constructed environments: A physical and numerical comparison of free-surface elevation, velocity, and momentum flux. Coastal Eng., 79, 9-21.

Rueben, M., Holman, R., Cox, D.T., Shin, S., Killian, J. and Stranley, J., 2011. Optical measurements of tsunami inundation through an urban waterfront modeled in a large-scale laboratory basin. Coastal Eng., 58, 229-238.

Soares-Frazao, S., Zech, Y. (2008): "Dam-break flow through an idealized city" J Hydrauic Res, 46(5), 648-658.

Sridhar, A. (2018): "Large-eddy Simulation of Turbulent Boundary Layers with Spatially Varying Roughness" PhD Thesis, California Institute of Technology, Pasadena, California.

Wang, X., Liu, P.L.-F.., 2011. "An explicit finite difference model for simulating nonlinear and weakly dispersive waves over slowly varying water depth" Coastal Engineering, 58(2), 173-183.

Yeh, H., Barbosa, A.R., Ko, H., Cawley, J. (2014): "Tsunami Loadings on Structures-Review and Analysis" Coastal Engineering Proceedings, 2014.

Younis, M.Y., Alam, M.M., Zhou, Y. (2016): "Flow around two non-parallel tandem cylinders" Phys. Fluids, 28, 125106.